# A novel discrete phase solver for high-speed spray simulations in industrial applications

Marcel Diviš[1*], Evgeniy Shapiro[2], David Einšpigel[1]

[1]Ricardo Software, Ricardo Prague s.r.o., Praha, Czech Republic
[2]Ricardo Software, Ricardo UK Ltd, Shoreham–by–Sea, United Kingdom

*Corresponding author: marcel.divis@ricardo.com

## Abstract

A novel feature-rich discrete phase solver is presented and its applications to high-speed liquid sprays are discussed. The solver has been implemented in the 3D CFD VECTIS suite, which is a tool for solving advanced industrial fluid flow problems. Eulerian/Lagrangian representation has been adopted for the analysis of the two-phase flows with the discrete phase statistically grouped in computational parcels. The solver features a set of detailed physical sub-models which are particularly suitable for high-speed sprays, namely the droplet evaporation, aerodynamic drag and heat transfer, primary and secondary breakup and droplet impingement models.

The integration of the discrete phase is based on an advanced face-to-face tracking algorithm with variable time step control used to maximise the efficiency of the time integration of the parcel balance equations. The time step is chosen individually for each parcel based on the particle response times in the mass, momentum and energy balances. This ensures that the time resolution of the solution is sufficient for an accurate prediction of the inter-phase transfer processes. The phase coupling is an important issue for modelling of highly separated two-phase flows. A kernel-function approach has been used in the code for the evaluation of continuous flow properties at droplet positions as well as for the distribution of the sources from droplets to their gaseous surroundings. This approach minimises undesirable effects of the computational grid on the spray formation prediction. The code adopts an up-to-date approach to the spray breakup modelling. A hybrid breakup model improves the accuracy of the breakup predictions for a wide range of conditions found in high-speed sprays by combining two breakup models. The variable time stepping approach has been extended to take into account the droplet characteristic breakup time.

The implemented solver has been applied to a number of test cases with different injector geometries and with injection pressures up to the level typical for modern diesel engines. The predicted spray structures were validated with experimental data demonstrating good accuracy of the spray solver. The computational costs of the discrete phase solver have been found to be reasonable by comparison with the overall cost of the 3D flow solution.

## Keywords

two-phase flows, discrete phase solver, particle tracking, spray break-up, engine sprays

## Introduction

Discrete phase modelling in computational fluid dynamics has been subject of continuous research over the past three decades. Despite the accuracy of predictions having improved significantly, it is still regarded as a challenge due to the complexity of the processes involved. In practical engineering applications, it is impossible to resolve directly all the details of the flow. Approximate sub-models are needed to account for the processes taking place on sub-grid scales. This necessarily introduces a certain level of empiricism and makes the results not entirely predictive.

Spray processes are frequently encountered in a variety of industrial applications at a wide range of operating conditions. Among them one of the most advanced applications is the internal combustion engine. Driven by climate concerns, ever-tightening requirements for maximum fuel economy and minimum emissions have lead to a rapid development of advanced combustion concepts. The predominant method of controlling the fuel mixture preparation in majority of today engines is refining the liquid fuel injection. This has been accompanied by ever-increasing injection pressures which poses a serious challenge to the numerical simulations of the two-phase flows with rapid spatial and temporal flow variations, significant inter-phase velocity and temperature differences and intense heat, momentum and mass transfer rates. These challenges make engine spray applications an excellent choice when assessing a discrete phase solver.

In this work, the Eulerian/Lagrangian representation of two-phase flow has been adopted. This approach has been the industrial standard for simulations of two-phase flows with discrete particles dispersed in the continuous fluid due to its efficiency and clear interpretation of the underlying physics, see e.g. [6, 2].

## Dispersed phase governing equations

The governing equations of particle motion are fundamental to the development of a discrete phase solver in Lagrangian framework. The primary application of the model is engine sprays, where the following basic assumptions are commonly adopted:

- discrete phase is in the form of small, homogeneous, spherically symmetric particles,

- discrete phase density is significantly higher than the continuous phase density,
- two-phase flow is highly separated – significant slip velocities between the phases.

Nevertheless, extensions of approaches developed for engine sprays to other applications, e.g. bubble flows, are possible through introduction of appropriate terms into the governing equations presented below. In the present work, the governing equations are described for chemically homogeneous (single-component) particles for simplicity. However an extension of the model based on a multi-component liquid mixture model published in [5] is already available in VECTIS-MAX.

### *Particle mass balance*

Under the above-mentioned assumptions, the mass balance of an evaporating droplet can be written as,

$$\frac{dm_D}{dt} = \dot{m}_{EV} = -\pi D \rho_F \mathscr{D} Sh \ln \frac{1 - Y_G}{1 - Y_{D,s}}. \tag{1}$$

Assuming constant fluid properties, re-arrangement and integration of the equation yields so-called $D^2$–law,

$$D^2 = D_0^2 - \Lambda_E t, \qquad \Lambda_E = 4\mathscr{D} Sh \frac{\rho_F}{\rho_D} \ln \frac{1 - Y_G}{1 - Y_{D,s}}. \tag{2}$$

The characteristic time for droplet evaporation can be estimated as the droplet lifetime. Comparison of the evaporation parameter $\Lambda_E$ with RHS of Eq. (1) then yields,

$$\tau_E = \frac{D^2}{\Lambda_E} = \frac{3}{2} \frac{m_D}{\dot{m}_{EV}}. \tag{3}$$

### *Particle momentum equation*

Taking into account given application, the main forces acting on a particle (droplet) are the aerodynamic drag force, a body force (gravity), and the buoyancy force. The equation of motion for both solid particles and evaporating droplets can be written as,

$$\frac{d\vec{r}_D}{dt} = \vec{w}_D, \tag{4}$$

$$m_D \frac{d\vec{w}_D}{dt} = -\vec{F}_D + m_D \vec{g} - \rho_G V_D \vec{g}. \tag{5}$$

Further simplification of the above equation is possible through introduction of the particle momentum response time $\tau_M$,

$$\frac{d\vec{w}_D}{dt} = -\frac{\vec{w}_D - \vec{w}_G}{\tau_M} + \left(1 - \frac{\rho_G}{\rho_D}\right)\vec{g}, \qquad \tau_M = \frac{4}{3} \frac{\rho_D D}{c_D \rho_G |\vec{w}_D - \vec{w}_G|}. \tag{6}$$

For spherical particles, the drag coefficient, $c_D$, suggested by [17] or [19] can be used. Deforming droplets can be considered using the approach published in [10].

### *Particle energy equation*

Taking into account simultaneous heat and mass transfer (Stefan's flow), particle energy equation can be written as,

$$m_D \frac{dc_{p,D} T_D}{dt} = -\pi Nu F_Z \lambda_F D(T_D - T_G) + h_{fg} \frac{dm_D}{dt}, \tag{7}$$

where the correction to the heat transfer rate, $F_Z$, due to the evaporation from the droplet surface is estimated according to [21]. By introducing particle thermal response time, the above equation can be re-written to,

$$\frac{dT_D}{dt} = -\frac{T_D - T_G}{\tau_H} + \frac{h_{fg}}{m_D c_{p,D}} \frac{dm_D}{dt}, \qquad \tau_H = \frac{\rho_D c_{p,D} D^2}{6 Nu F_Z \lambda_F}. \tag{8}$$

### Break-up modelling

For high-speed sprays, spray break-up is an important process that greatly influences spray formation. A hybrid break-up model used in this work is a further extension of the model developed in [4]. It attempts to improve the accuracy of the break-up predictions for high-speed sprays by combining two break-up models. The first break-up model is used in the primary break-up region of the spray, where the initial continuous liquid jet disintegrates into ligaments and droplets. In the downstream region of the spray, the second break-up model is used to predict further breakup of the droplets.

A switching criterion is needed to decide which break-up model should be employed for a given droplet parcel. In this work, all droplet parcels with the distance from the nozzle orifice exit shorter than a spray break-up length are treated with the first break-up model. Droplet parcels that have already travelled beyond that distance are treated with the second break-up model. The spray break-up length is estimated using the correlation proposed by Levich [9],

$$L_B = 5.5 D_{INJ} \sqrt{\frac{\rho_D}{\rho_G}}. \tag{9}$$

### Instability analysis

The breakup prediction within the breakup length region is done assuming that injected liquid jets become unstable through Kelvin–Helmholtz instability. The continuous liquid jet is approximated by an injection of initial blobs. The blob size is then reduced gradually in each time step due to shedding of secondary droplets. This approximates the real primary break-up process under high jet velocities, where small droplets are gradually shed from the disturbed liquid jet surface.

The model is based on the well-known linear instability analysis of a cylindrical liquid jet injected into an incompressible gas developed in [10]. A curve fit of the numerical solution for the fastest growing wave of the Kelvin–Helmholtz instability was developed in [10]. The model was further elaborated in [14], where small child droplets are shed from blobs when the break-up occurs.

In the region beyond the breakup length, competing influences of both Rayleigh–Taylor and Kelvin–Helmholtz instabilities are taken into account. Secondary droplet size is supposed to decrease gradually in each time step until the droplet reaches its stable size. Kelvin-Helmholtz instability is calculated as described in the previous section. For Rayleigh–Taylor instability, following [22], the frequency of the fastest growing wave, $\Omega_{RT}$, corresponding wavelength, $\Lambda_{RT}$, and wave number, $K_{RT}$, are computed as follows,

$$\Omega_{RT} = \sqrt{\frac{2}{3\sqrt{3\sigma}}\frac{[a(\rho_D - \rho_G)]^{3/2}}{\rho_D + \rho_G}}, \qquad \Lambda_{RT} = 2\pi\frac{B_3}{K_{RT}}, \qquad K_{RT} = \sqrt{\frac{a(\rho_D - \rho_G)}{3\sigma}}. \tag{10}$$

The acceleration of the droplet is calculated as $a = |\vec{w}_D - \vec{w}_G|/\tau_M$

### Break-up rate prediction

With the maximum wave growth rates, $\Omega$, and the corresponding wave lengths, $\Lambda$, for both Kelvin–Helmholtz and Rayleigh–Taylor instabilities available, it is possible to predict the breakup time and the corresponding stable droplet size,

| Kelvin–Helmholtz | Rayleigh–Taylor | |
|---|---|---|
| $\tau_{B,KH} = \dfrac{3.788 B_1 D}{2\Omega_{KH}\Lambda_{KH}}$ | $\tau_{B,RT} = \dfrac{B_{RT}}{\Omega_{RT}}$ | (11) |
| $D_{stab,KH} = 2B_0\Lambda_{KH}$ | $D_{stab,RT} = \Lambda_{RT} = 2\pi B_3\sqrt{\dfrac{3\sigma}{a(\rho_D - \rho_G)}}$ | |

$B_0$, $B_1$, $B_{RT}$ and $B_3$ are the model parameters with the default values according to [14, 22] equal to $0.6$, $13$, $1$ and $5.3$, respectively. For both breakup modes, the size of a droplet undergoing break-up is supposed to reduce gradually in each computational time step to its stable size according to the well-known break-up rate expression suggested in [18],

$$\frac{dD}{dt} = -\frac{D - D_{stab}}{\tau_B}. \tag{12}$$

Within the breakup length region, the shed droplets create a new parcel with the droplet number $N_C$ and diameter $D_C$. The remaining liquid mass in the parent droplet parcel is re-grouped to create an updated parcel with the droplet number $N_N$ and diameter $D_N$. As this process should correspond to the break-up rate predicted by Eq. (12), the equations for mass and Sauter mean diameter conservation are used,

$$ND^3 = N_N D_N^3 + N_C D_C^3, \qquad D = \frac{N_N D_N^3 + N_C D_C^3}{N_N D_N^2 + N_C D_C^2}. \tag{13}$$

In order to limit the total number of generated droplet parcels, the child droplet parcels are only created if the mass of the predicted child parcel reaches at least 3% of the initial mass of the parent droplet parcel.

### Numerical solution

Assuming constant fluid properties within the particle integration time $\Delta t_D$, the RHS of the particle mass balance, see Eq. (1), is a function of the particle diameter. The integration is done in two stages using the trapezoidal rule with the Euler's first-order predictor.

$$\frac{m_D^{(n+1/2)} - m_D^{(n)}}{\Delta t_D} = \dot{m}_{EV}^{(n)}, \tag{14}$$

$$\frac{m_D^{(n+1)} - m_D^{(n)}}{\Delta t_D} = \frac{1}{2}\left(\dot{m}_{EV}^{(n+1/2)} + \dot{m}_{EV}^{(n)}\right). \tag{15}$$

A semi-implicit time integration is employed for both momentum and energy equations, see Eq. (6) and (8),

$$\frac{\vec{w}_D^{(n+1)} - \vec{w}_D^{(n)}}{\Delta t_D} = -\frac{\vec{w}_D^{(n+1)} - \vec{w}_G^{(n)}}{\tau_M} + \left(1 - \frac{\rho_G}{\rho_D}\right)\vec{g}, \tag{16}$$

$$\frac{T_D^{(n+1)} - T_D^{(n)}}{\Delta t_D} = -\frac{T_D^{(n+1)} - T_G^{(n)}}{\tau_H} + \frac{2h_{fg}}{c_{p,D}\Delta t}\frac{m_D^{(n+1)} - m_D^{(n)}}{m_D^{(n+1)} + m_D^{(n)}}. \tag{17}$$

The break-up rate equation, see Eq. (12), formally corresponds to the particle momentum and energy balances, see Eq. (6) and Eq. (8), and thus, it is solved in the same manner,

$$\frac{D^{(n+1)} - D^{(n)}}{\Delta t_D} = -\frac{D^{(n+1)} - D^{(n)}_{stab}}{\tau_B}. \tag{18}$$

The time step of the particle integration, $\Delta t_D$, is usually much smaller than that of the continuous phase integration and is adjusted dynamically along the particle trajectory. The time step is limited due to a number of physical restrictions:

- *particle residence time* $\tau_R = |\vec{r}_D - \vec{r}_F|/|w_D|$, for Face-to-Face particle tracking algorithms, the integration time is restricted by the Courant criteria to avoid traversing of more than one cell boundary.

- *response times*, $\tau_E, \tau_M, \tau_H$, see Eq. (3), (6) and (8), which correspond to the time scales of particle response to the changes in the respective flow properties,

- *breakup time*, $\tau_B$, that corresponds to the time scale of the droplet breakup process.

The particle integration time is thus chosen as,

$$\Delta t_D = \min(B_R \tau_R, B_E \tau_E, B_M \tau_M, B_H \tau_H, B_B \tau_{B,KH}, B_B \tau_{B,RT}), \tag{19}$$

where all the constants $B_X < 1$ can be adjusted by the user. More restrictions can be imposed on the particle integration time if further physical sub-models are employed, for instance a particle–eddy interaction time.

**Phase coupling**

The primary application of the model is high-speed sprays in automotive applications with highly separated two-phase flows and rapid inter-phase exchange of mass, momentum and energy. The two-way coupling needs thus be considered to account appropriately for the interaction between the phases.

***Continuous flow field interpolation***

Flow properties at the particle locations necessary for the solution of the discrete phase governing equations should be recovered from cell–centred data of the continuous phase. To accomplish this, several interpolation approaches have been proposed in the past including piecewise-constant interpolation, inverse distance weighting, tetrahedral split and kernel functions, see [13, 20, 11]. In the current work, the kernel function approach is used.

The continuous flow quantity $\phi_G$ at the particle location is calculated as a weighted average of the cell centre values,

$$\phi_G = \sum_i \omega_i \phi_i, \qquad \omega_i = \frac{K(\xi_i)}{\sum_j K(\xi_j)}, \qquad \xi_i = \frac{|\vec{r}_D - \vec{r}_i|}{b}, \qquad \xi_j = \frac{|\vec{r}_D - \vec{r}_j|}{b} \tag{20}$$

The indices $i$ and $j$ will theoretically run over all cells. A suitable choice of the kernel function shape, $K(\xi)$, ensures that only neighbouring cells need be examined. The normalisation done in Eq. (20) ensures that $\sum \omega_i = 1$ for any form of the kernel function. The Gaussian function is a reasonable candidate. However, the following kernel function is recommended in [23] due to efficiency considerations,

$$K(\xi) = \begin{cases} (1 - \xi^2)^4 & \text{for} \quad \xi < 1, \\ 0 & \text{for} \quad \xi \geq 1. \end{cases} \tag{21}$$

The choice of the bandwidth, $b$, influences the number of cells that are examined. Taking $b$ between $1.5\Delta x$ and $2.5\Delta x$ with $\Delta x$ being the average cell size appears to be a suitable choice.

***Inter-phase source terms***

The coupling between the discrete and continuous phase is done through introduction of source terms in the continuous flow governing equations. For instance, the source therm for the gas flow continuity equation due to the discrete phase evaporation is given by,

$$\vec{S}_{G,E} = \frac{1}{\Delta t_G} \sum_k \left[ \sum_n N_{D,k} \left( m^{(n)}_{D,k} - m^{(n+1)}_{D,k} \right) \right] \tag{22}$$

where the particles are statistically grouped into so-called parcels, each of which containing a number of particles, $N_D$. The index $k$ runs over the number of parcels traversing the cell within given time step, $\Delta t_G$, and the index $n$ runs over the number of particle time steps, $\Delta t_D$, necessary to complete the integration of the particle in given cell within the gas flow time step, $\Delta t_G$. The source terms for the momentum and energy equations are defined in the same manner.

### *Source terms distribution*

The source term in Eq. (22) is defined by summing the momentum source contributions from all droplet parcels traversing the investigated cell within given time step. As an alternative, a more accurate method is also provided taking into account the actual position of the droplet parcel within the computational grid formulated using kernel functions. The contribution of a droplet parcel to the gas flow source is then applied not only to the droplet residence cell but also to the neighbouring cells based on the relative distance from the particle location to the cell centres. The above-mentioned approach is suggested in [8] using a quadratic function. Importance of the momentum source term distribution not only over the particle residence cell is stressed in [7]. The source terms are distributed over the neighbouring cells in the same way as the gas flow properties are interpolated, see Eq. (20), using the same shape of the kernel function (Eq. (21)).

### Particle tracking

Methods for tracking Lagrangian particles on a fixed or moving gas-phase computational mesh can be broadly classified into two families - Lose-Find (LF) and Face-to-Face (F2F) (e.g. [13, 3]). The LF approach integrates the equation of motion explicitly within the time-step defined by the governing equations of particle motion and their associated constraints. Following the integration, the end position of the particle is found on the computational mesh. LF algorithms can be suitable for small time steps usually imposed by the Lagrangian solver and are arguably easier to implement. However the simplicity of LF algorithms does not extend easily to parallel simulations, where implementation of an efficient search for the endpoint of particle trajectory requires complex data structures and is computationally expensive. Furthermore, potential problems with parcels jumping over cells without interacting with them leads to additional restrictions on the simulation Courant number. By contrast, F2F algorithms follow the particle path by determining exit points of the particle trajectory in each cell, thus the resident cell of the particle and the proportion of the trajectory residing in a given cell traversed by the particle are always known. However, explicit F2F integration of the equations of motion with the adjustment of trajectory at each cell face intersection (e.g. [12])) can introduce additional grid sensitivity into the solution. The tracking algorithm developed in VECTIS-MAX aims to combine both approaches, resulting in the procedure described below.
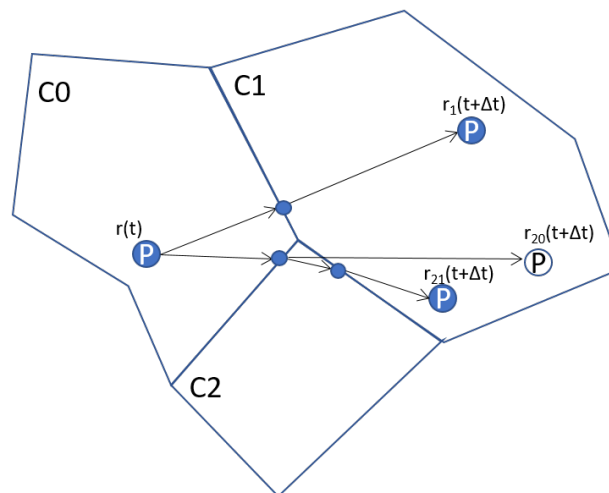


**Figure 1.** Particle tracking schematic

Consider a particle $P$ travelling from cell C0 where its position at time $t$ is given by $r(t)$. Fig. 1 illustrates two possible scenarios in 2D for simplicity. In both scenarios, the end points $r_1(t + \Delta t)$ and $r_{20}(t + \Delta t)$ are located cell C1. However in the first one the trajectory is fully contained within the cells marking the start and end points of particle integration, whereas in the second scenario, the trajectory traverses a portion of cell C2. The algorithm proceeds as follows:

- Cell-segment intersection analysis is performed based on the current and projected particle end position and star triangulation of cell C0's faces. Resulting in an exit face and the proportion of the trajectory residing in cell C0 stored for source terms calculation. Star triangulation of the faces is done on the fly, but the face centroids are readily available from the gas-phase solver.

- Scenario 1: The target cell C1 is determined as the exit face neighbour sharing face $x_1$ and a fast ray-tracing search confirms that cell C1 contains the final destination of the particle $r_1(t + \Delta t)$. The particle position and residence cells are updated. The proportion of trajectory belonging to cell C1 has been already computed in the previous step and is available for source terms calculation. Note that in this scenario, which is most typical in simulations, traversing a face does not alter the integration of particle's equations of motion.

- Scenario 2: Cell C2, the exit face neighbour of face $x_2$ does not contain the end point of the predicted trajectory $r_{20}(t + \Delta t)$. An automatic Courant number correction is performed by splitting the particle trajectory

and integrating equations of motion again with the intersection point with face $x_2$ as a starting point (as in [12]), resulting in a modified end position $r_{21}(t + \Delta t)$ and proportions of trajectory residing in cells C2 and C1 respectively.

The above algorithm deals gracefully with warped faces and complex concave shapes of cells. It also yields itself easily to parallel implementation within a domain decomposition/MPI approach and has been tested extensively on various types of grids supported in VECTIS-MAX. It is worth noting that particles with trajectories traversing a cell edge do not pose a problem as the identical ordering of face triangles for point-in-cell problem on both sides of the face forms watertight volumes even when a tolerance is used to decide which side of an edge the trajectory is intersecting. A particle trajectory traversing through a corner point shared by multiple cells can still result in a particle being lost as re-positioning to a face intersection point might fail. In such cases, search for the re-positioned particle has to be extended, however with application of shoe-boxing within each parallel partition, the detriment to performance of such rare extended searches has been observed to be negligible.

## Results and discussion

The developed discrete phase solver has been implemented into a commercial 3D CFD program VECTIS-MAX, which is a tool for solving advanced industrial fluid flow problems, see [15, 16]. Examples of the simulations carried out in order to test the overall code performance and accuracy are presented in this section.

### *Non-evaporating sprays*

Based on experiments by Allocca et al. [1], a single-hole nozzle injection using a diesel type injector has been simulated. Liquid tetradecane is injected into a vessel at room temperature and an elevated gas pressure, see the conditions summarised in Tab. 1. As evaporation is suppressed under given conditions, the test case is suitable for a validation of the break-up models and spray–gas momentum coupling. Results of the simulation and experimental data are compared using the spray liquid penetration. The simulated liquid penetration is defined as a distance from the nozzle outlet to the farthest position encompassing 95% of the injected mass. The results are shown in Fig. 2. The agreement of the simulation with the experiment is excellent.

**Table 1.** The basic conditions of the single-hole nozzle spray simulations according to [1]

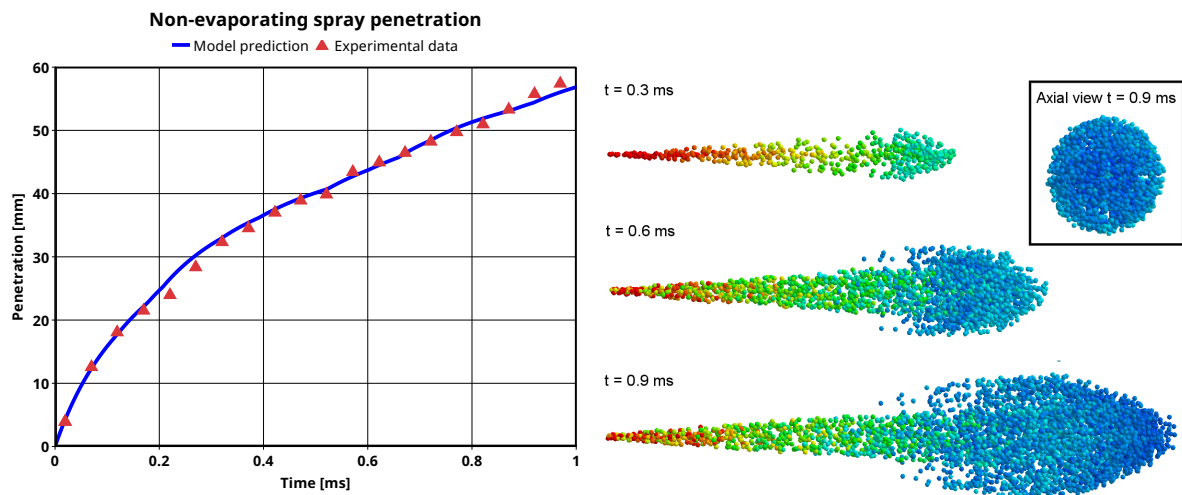| | |
|---|---|
| Nozzle orifice diameter | 0.2 mm |
| Maximum injection pressure | 100 MPa |
| Ambient gas pressure | 1.7 MPa |
| Ambient gas temperature | 300 K |



**Figure 2.** The simulated and experimental liquid penetrations and simulated spray plumes at various times after start of injection (t = 0.3, 0.6, 0.9 ms).

In addition, there are no apparent grid artefacts in the side and axial views of the spray in Fig. 2. Grid artefacts are common for simulated sprays if the exchange of flow properties between a particle and continuous flow is done solely through the particle residence cell. An asymmetric spray formation aligned with grid principal axes is often obvious. In the developed model, the use of kernel functions for the evaluation of continuous flow properties as well as for the distribution of discrete-phase source terms to the continuous flow reduces significantly the influence of underlying Cartesian grid on the spray formation.

### *Evaporating sprays*

A single-orifice nozzle injection at elevated pressure and temperature has been simulated based on the well-known *Spray A* from the Engine Combustion Network, see [24]. An overview of the experimental conditions is given in Tab. 2. In Fig. 3, simulation results are compared with the experimental data using the spray liquid and vapour penetrations. The simulated vapour penetration is defined as a maximum distance from the nozzle outlet where the fuel mass fraction exceeds 0.1%. Fig. 4 shows simulated and experimental gas velocity profiles in radial direction at 40 mm from the injector exit. The agreement of the simulation results with the experiment is very good in all cases.
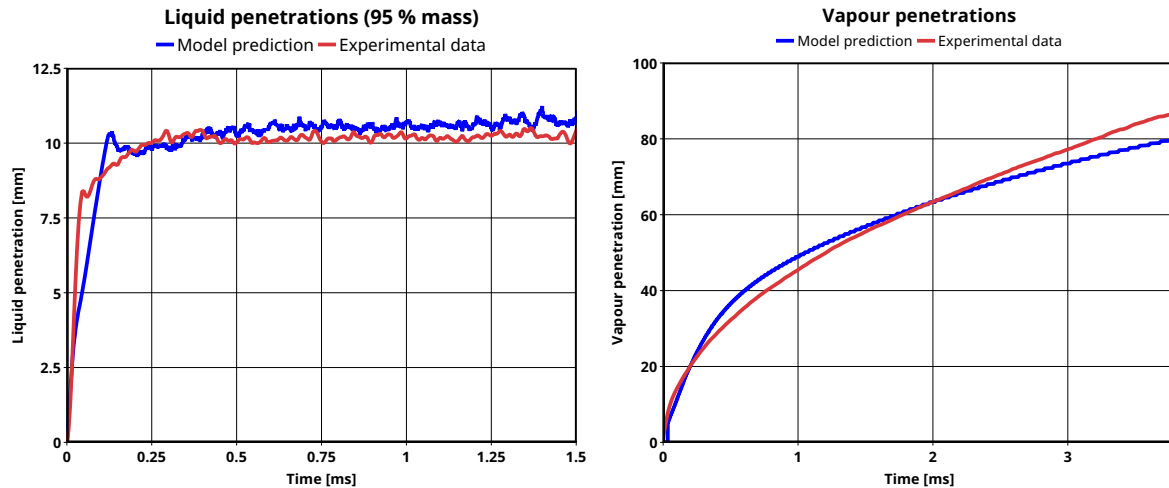


**Figure 3.** The simulated and experimental liquid (left) and vapour (right) penetrations for ECN *Spray A* case.

The relative costs of the discrete phase solution differ significantly in dependency on both the computational grid geometry and the injection set-up. Nevertheless, for given case, the overall time spent by discrete phase solver accounts for only ~2% of the total computational time.

**Table 2.** The basic conditions of the ECN *Spray A* simulations according to [24].

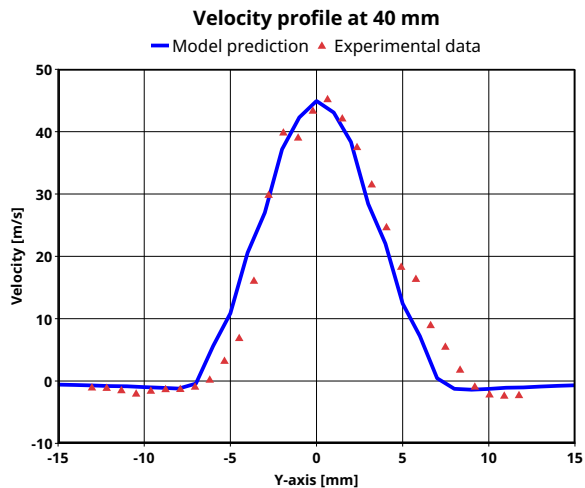| | |
|---|---|
| Nozzle orifice diameter | 0.09 mm |
| Fuel injection pressure | 150 MPa |
| Fuel temperature at nozzle | 363 K |
| Fuel | n-dodecane |
| Ambient gas pressure | 6.0 MPa |
| Ambient gas temperature | 900 K |



**Figure 4.** The simulated and experimental gas velocity profiles at 40 mm from the injector for ECN *Spray A* case.

### Conclusions

A novel feature-rich Lagrangian discrete phase solver has been developed and applied to high-speed liquid sprays simulations. The solver has been implemented in VECTIS-MAX, a the 3D CFD tool for solving advanced industrial fluid flow problems. The solver features a set of detailed physical sub-models which are particularly suitable for high-speed sprays.

Up-to-date approaches to the spray breakup modelling are adopted. The hybrid breakup model improves the accuracy of the breakup predictions for a wide range of conditions found in high-speed sprays by combining two breakup models. A kernel-function approach has been used for evaluation of the coupling between the discrete phase and continuous flow which minimises undesirable effects of the computational grid on the spray formation prediction. To maximise the efficiency of the time integration of the discrete phase equations, an advanced face-to-face tracking algorithm with a variable time step control based on the particle response times has been implemented.

The computational costs of the discrete phase solver have been found to be reasonable by comparison with the overall cost of the 3D flow solution.

The implemented solver has been applied to a number of test cases with different injector geometries and with the injection pressures up to the level typical for modern diesel engines. The predicted sprays were validated with experimental data demonstrating good accuracy of the discrete phase solver.

## Nomenclature

| | | | |
|---|---|---|---|
| $a$ | acceleration [m s$^{-2}$] | $\Lambda_E$ | evaporation parameter [m$^2$ s$^{-1}$] |
| $A$ | area [m$^2$] | $\xi$ | bandwidth [m] |
| $B$ | model parameter [-] | $\mu$ | dynamic viscosity [Pa s] |
| $c_P$ | isobaric specific heat [J (kg K)$^{-1}$] | $\rho$ | density [kg m$^{-3}$] |
| $C_D$ | droplet drag coefficient [-] | $\sigma$ | surface tension [N m$^{-1}$] |
| $D$ | diameter [m] | $\tau$ | time [s] |
| $\mathscr{D}$ | binary diffusion coefficient [m$^2$ s$^{-1}$] | $\Omega$ | wave growth rate [s$^{-1}$] |
| $\vec{F}$ | force [N] | Subscripts | |
| $F_Z$ | heat transfer rate correction factor [-] | $0$ | initial condition |
| $\vec{g}$ | body force acceleration [m s$^{-2}$] | $B$ | break-up |
| $h_{fg}$ | specific enthalpy of vaporisation [J kg$^{-1}$] | $C$ | child droplet |
| $K$ | wave number [m$^{-1}$] | $D$ | droplet |
| $L_B$ | break-up length [m] | $D,s$ | droplet surface |
| $m$ | mass [kg] | $F$ | film conditions |
| $\dot{m}_{EV}$ | droplet mass evaporation rate [kg s$^{-1}$] | $G$ | gas |
| $N$ | droplet number [-] | $INJ$ | injection nozzle |
| $\vec{r}$ | positional vector [m] | $i,j$ | gas cell indices |
| $t$ | time [s] | $k$ | droplet parcel index |
| $\vec{w}$ | velocity [m s$^{-1}$] | $KH$ | Kelvin–Helmholtz instability |
| $Y$ | mass fraction [-] | $n$ | time step index |
| $\Delta t$ | time step [s] | $N$ | updated droplet parcel |
| $\phi$ | generic quantity [-] | $RT$ | Rayleigh–Taylor instability |
| $\lambda$ | thermal conductivity [W (m K)$^{-1}$] | $stab$ | stable droplet |
| $\Lambda$ | wavelength [m] | | |

## References

[1] Allocca, L., Belardini, P., Bertoli, C., Corcione, F. E., and Angelis, F. D., 1992, SAE Technical Paper 920576.

[2] Amsden, A. A., O'Rourke, P. J., Butler, T. D., 1989, Technical Report LA-11560-MS, Los Alamos National Laboratory, Los Alamos, USA.

[3] Chorda R., Blasco J.A. and Fueyo N., 2002, International Journal of Multiphase Flow 28, pp. 1565–1580.

[4] Diviš, M., 2016, 27th European Conference on Liquid Atomization and Spray Systems.

[5] Diviš, M., Tiney, N. K., Lucas, G., 2016, VPC – Simulation and Test 2016.

[6] Dukowicz, J. K., 1980, *Journal of Computational Physics*, 35, pp. 229–253.

[7] Franklin, J. D., 2012, *Powder Technology*, 220, pp. 88–97.

[8] Hammerl, G., Wall, W. A., 2015, *Journal of Physics: Conference Series*, 656.

[9] Levich, V. G., 1962, "Physicochemical hydrodynamics". Prentice-Hall.

[10] Liu, A. B., Mather, D. and Reitz, R. D., 1993, SAE Technical Paper 930072.

[11] Lucchini, T., D'Errico, G., Ettorre, D., 2011, *International Journal of Heat and Fluid Flow*, 32, pp. 285–297.

[12] Macpherson G. B., Nordin N. and Weller H. G., 2002, Commun. Numer. Meth. Engng. 25, pp. 263–273.

[13] Nordin, N., 2001, "Complex Chemistry Modeling of Diesel Spray Combustion", Ph.D. thesis, Chalmers University of Technology.

[14] Patterson, M. A. and Reitz, R. D., 1998, SAE Technical Paper 980131.

[15] Pržulj, V., Birkby, P., Mason, P., May 11.-16. 2008, Advances in Computational Heat Transfer, CHT-08.

[16] Pržulj, V., Penning, R., Tiney, N., July 01.-06. 2012, Advances in Computational Heat Transfer, CHT-12.

[17] Putnam, A., 1961, *ARS Journal*, 31, pp. 1467–1468.

[18] Reitz, R. D. and Diwakar, R., 1987, SAE Technical Paper 870598.

[19] Schiller, L., Naumann, A., 1933, *VDI Zeits*, 77, p. 318.

[20] Schmidt, D. P., Senecal, P. K., 2002, SAE Technical Paper 2002-01-1113.

[21] Wakill, M. M. E., Ueyhara, O. A. and Myers, P. S., 1954, NACA Technical Note 3179, NACA.

[22] Wang, Y., Ge H.-W. and Reitz, R. D.,2010, SAE Technical Paper 2010-01-0626.

[23] Xiao, H., Sun, J., 2011, *Communications in Computational Physics*, 9 (2), pp. 297–323.

[24] Engine Combustion Network: "Spray A" and "Spray B" Operating Condition, https://ecn.sandia.gov/diesel-spray-combustion/target-condition/spray-ab/ ([cit. 2019-03-11]).